The Astrophysical Journal, 979:189 (15pp), 2025 February 1 https://doi.org/10.3847/1538-4357/ad9e93

The Observed Phase Space of Mass-loss History from Massive Stars Based on Radio Observations of a Large Supernova Sample

Itai Sfaradi[1], Assaf Horesh[1], Rob Fender[2], Lauren Rhodes[2], Joe Bright[2], David Williams-Baldwin[3], and Dave A. Green[4]
[1] Racah Institute of Physics, The Hebrew University of Jerusalem, Jerusalem 91904, Israel; itai.sfaradi@berkeley.edu
[2] Astrophysics, Department of Physics, University of Oxford, Keble Road, Oxford, OX1 3RH, UK
[3] Jodrell Bank Centre for Astrophysics, School of Physics and Astronomy, The University of Manchester, Manchester, M13 9PL, UK
[4] Astrophysics Group, Cavendish Laboratory, 19 J. J. Thomson Avenue, Cambridge, CB3 0HE, UK
Received 2024 July 17; revised 2024 November 22; accepted 2024 December 2; published 2025 January 27

Abstract

In this work, we study the circumstellar material (CSM) around massive stars, and the mass-loss rates depositing this CSM, using a large sample of radio observations of 325 core-collapse supernovae (CCSNe; only ~22% of them being detected). This sample comprises both archival data and our new observations of 99 CCSNe conducted with the AMI-LA radio array in a systematic approach devised to constrain the mass loss at different stages of stellar evolution. In the supernova (SN)–CSM interaction model, observing the peak of the radio emission of an SN provides the CSM density at a given radius (and therefore the mass-loss rate that deposited this CSM). On the other hand, limits on the radio emission, and/or on the peak of the radio emission provide a region in the CSM phase space that can be ruled out. Our analysis shows a discrepancy between the values of mass-loss rates derived from radio-detected and radio-nondetected SNe. Furthermore, we rule out mass-loss rates in the range of 2×10^{-6}–$10^{-4}\,M_{\odot}\,\mathrm{yr}^{-1}$ for different epochs during the last 1000 yr before the explosion (assuming wind velocity of $10\,\mathrm{km\,s}^{-1}$) for the progenitors of ~80% of the Type II supernovae (SNe II) in our sample. In addition, we rule out the ranges of mass-loss rates suggested for red supergiants for ~50% of the progenitors of SNe II in our sample. We emphasize here that these results take a step forward in constraining mass loss in winds from a statistical point of view.

Unified Astronomy Thesaurus concepts: Core-collapse supernovae (304); Massive stars (732); Circumstellar matter (241); Radio astronomy (1338); Time domain astronomy (2109)

Materials only available in the online version of record: machine-readable tables

1. Introduction

Mass loss from massive stars, stars with $M_{\mathrm{ZAMS}} \geqslant 8M_{\odot}$, can be significant and affect their luminosity, lifetime, composition, and mass. Toward the end of its life, mass loss from a massive star can strongly influence the fate of the star and the resulting supernova (SN; N. Smith 2014). Various models and observations suggest ranges of mass-loss rates for massive stars during different phases of their evolution (e.g., C. de Jager et al. 1988; J. S. Vink et al. 2001; N. Langer 2012; N. Smith 2014; J. S. Vink 2022; I. Irani et al. 2023). However, mass loss at the last stages of stellar evolution is still unconstrained empirically.

Type II (hydrogen-rich) supernovae (SNe II) and their variations (II-L, II-P, IIn; excluding Type IIb), and stripped-envelope SNe (Types IIb, Ib, and Ic; hydrogen-poor) are associated with the death of massive stars as they reach the evolutionary point when nuclear burning can no longer provide support against the star's own gravity. This stellar death can result in a core-collapse supernova (CCSN) explosion. In these explosions, stellar material is ejected at very high velocities reaching ~10,000 $\mathrm{km\,s}^{-1}$ for SNe II, and even higher ejecta velocities for stripped-envelope SNe (A. V. Filippenko 1997; A. Gal-Yam 2017; R. A. Chevalier & C. Fransson 2006). The interaction between the SN ejecta and the circumstellar material (CSM) generates the radio emission (R. A. Chevalier 1981, 1998; K. W. Weiler et al. 2002). The CSM closest to the star has been deposited via mass-loss processes (e.g., stellar winds and eruptive mass ejection) just before the explosion. Thus, early radio observations of young SNe reveal the environment of the progenitor at its final evolutionary stages and its mass-loss rate just before the explosion.

In the last four decades, an increasing number of SNe have been detected in radio, revealing surprising variations in spectra and light curves. While most stripped-envelope SNe exhibit clear self-absorbed synchrotron spectrum (R. A. Chevalier 1998), most SNe II point toward a spectrum associated with free–free absorption (e.g., SN 1979C (K. W. Weiler et al. 1991); SN 2023ixf (A. J. Nayana et al. 2024)). The radio luminosity–rise time relation of CCSNe was studied by M. F. Bietenholz et al. (2021) on a large sample of radio observation of CCSNe. Their analysis of all the SNe in their sample (detected and nondetected in radio wavelengths) suggests that the peak luminosity of SNe Ib, Ic, and II is ~$2 \times 10^{25}\,\mathrm{erg\,s}^{-1}\,\mathrm{Hz}^{-1}$, and that SNe Ib and Ic rise time is 12–15 days after the SN explosion, shorter than the ~30–100 days inferred for SNe II. Since SNe IIn present narrow lines in their optical spectrum, associated with the interaction with a dense CSM, they were excluded from this analysis. In addition, SNe IIb, presenting a transitional optical spectrum (initially showing hydrogen lines in the optical spectrum that disappear at late times), were also excluded from the analysis above. Based on these results, M. F. Bietenholz et al. (2021) inferred a mean mass-loss rate for the progenitors of SNe Ib and Ic of ~$4 \times 10^{-6}\,M_{\odot}\,\mathrm{yr}^{-1}$ (for an assumed constant mass-loss rate in steady winds of $1000\,\mathrm{km\,s}^{-1}$). For the progenitors of SNe II (excluding Type IIn), the inferred

mean of mass-loss rate is $\sim 10^{-7} M_{\odot}\,\mathrm{yr}^{-1}$ (for winds of $10\,\mathrm{km\,s}^{-1}$).

Some SNe, for example, SN 2014C (G. E. Anderson et al. 2017), exhibit multiple peaks in their radio light curve, suggesting that the SN ejecta interacts with two separate CSM shells deposited in two separate mass-loss stages. Some SNe (e.g., SN 2003L (A. M. Soderberg et al. 2005a); SN 2019oys (I. Sfaradi et al. 2024)) exhibit broad radio spectral peaks, which are associated with CSM inhomogeneities caused by variations in the distribution of relativistic electrons and/or the magnetic field strength within the synchrotron source. Fast shock waves (0.2–0.3c) traveling in a dense environment have been captured when observations were taken early enough (e.g., the SNe Ic—SN 2002ap (E. Berger et al. 2002); PTF12gz (A. Horesh et al. 2013b) and can link normal SNe Ic to relativistic ones (R. Margutti et al. 2014).

A typical assumption when studying the radio emission from CCSNe is that there is equipartition between the energy deposited in the relativistic electrons and in the magnetic fields (M. A. Scott & A. C. S. Readhead 1977; R. A. Chevalier 1998; R. Barniol Duran et al. 2013). Combined radio and X-ray observations (e.g., SN 2011dh (M. I. Krauss et al. 2012; A. M. Soderberg et al. 2012; A. Horesh et al. 2013c); SN 2013d (A. Kamble et al. 2016); SN 2020oi (A. Horesh et al. 2020)) displayed deviation from this equipartition (with a larger fraction of energy deposited in the relativistic electrons). Other early multiwavelength observations have shown the importance of electron cooling, including SN 2012aw (N. Yadav et al. 2014), in which the steep radio spectrum observed early on showed a significant inverse Compton cooling at frequencies above 1 GHz. In addition to this large variety of detected SNe, there are a lot more SNe that were observed and were not detected at radio wavelengths. A nondetection of an SN in radio can rule out a range of mass-loss rates from the progenitor star.

In this paper, we probe the CSM around massive stars (and the mass-loss rates depositing this CSM) from a population point of view, using radio observations of both radio-detected and nondetected CCSNe. We start by introducing the SN–CSM interaction model in Section 2. In Section 3, we describe the large sample of CCSNe observed in radio wavelengths, with new observations of CCSNe first introduced here. We analyze this sample in Sections 4 and 5 according to the model described in Section 2. In Section 6, we test our model assumptions and their impact on our conclusions. Section 7 contains our conclusions.

2. SN–CSM Interaction Model

In the SN–CSM interaction model (R. A. Chevalier 1981), the SN ejecta drives a shock wave into the CSM. At the shock front, particles are accelerated to relativistic velocities and gyrate in the presence of a magnetic field. These relativistic particles give rise to synchrotron emission, which is usually brightest at radio frequencies. While R. A. Chevalier (1998) showed that the early radio emission is fairly well described by a synchrotron self-absorption (SSA) model, free–free absorption (FFA; K. W. Weiler et al. 2002) can also take part. Next, we describe the model for the SSA spectrum and connect it to the density of the CSM and mass-loss rate from the progenitor. Then, we show the full model we use by introducing external FFA to the SSA spectrum.

In this model, the relativistic particles have an energy density distribution of $N(E) = N_0 E^{-p}$. As described in Equation (1) in R. A. Chevalier (1998), the flux density from an SSA spectrum at a frequency ν is given by

$$F_{\nu} = \frac{\pi R^2}{D^2}\left(\frac{\nu}{\nu_1}\right)^{5/2} \times \left(1 - \exp\left[-\left(\frac{\nu}{\nu_1}\right)^{-(p+4)/2}\right]\right), \quad (1)$$

where

$$\nu_1 = 2c_1\left(\frac{4}{3} f R c_6 N_0\right)^{2/(p+4)} B^{(p+2)/(p+4)},$$

R is the radius of the radio-emitting shell, B is the magnetic field strength, f is the emission filling factor, and D is the distance to the SN. The constants c_1, c_5, and c_6 can be found in A. G. Pacholczyk (1970). Since the total energy density in relativistic electrons is $\int_{E_1}^{\infty} N(E)\,dE$, where E_1 is the electron rest mass energy,[5] the equipartition assumption (M. A. Scott & A. C. S. Readhead 1977; R. A. Chevalier 1998) gives

$$N_0 = \frac{f_{\mathrm{eB}} B^2 (p-2) E_l^{p-2}}{8\pi}. \quad (2)$$

R. A. Chevalier & C. Fransson (2006) showed that one can estimate the radius of the emitting shell and the magnetic field strength at that time given the radio spectral peak flux density, F_{ν_a}, and frequency, ν_a. The radius is given by

$$R = \left[\frac{6 c_6^{p+5} F_{\nu_a}^{p+6} D^{2p+12}}{f_{\mathrm{eB}} f (p-2) E_1^{p-2} \pi^{p+5} c_5^{p+5}}\right]^{\frac{1}{2p+13}} \left(\frac{\nu_{\mathrm{a}}}{2c_1}\right)^{-1}, \quad (3)$$

and the magnetic field strength is

$$B = \left[\frac{36\pi^3 c_5}{f_{\mathrm{eB}}^2 f^2 (p-2)^2 E_1^{2(p-2)} c_6^3 F_{\nu_a} D^2}\right]^{\frac{2}{2p+13}} \left(\frac{\nu_{\mathrm{a}}}{2c_1}\right), \quad (4)$$

where f_{eB} is the ratio between the fraction of shock wave energy deposited in the relativistic electrons (ϵ_{e}) to the fraction of shock wave energy converted to the magnetic field (ϵ_{B}).

The temporal evolution of the radio spectrum is determined by the evolution of the radius and magnetic field with time. A typical assumption is of a free expansion of the shock, which dictates a constant shock velocity, $v_{\mathrm{sh}} = R/t$, where t is the time since the explosion. Assuming that a fraction (ϵ_{B}) of the post-shock thermal energy density, $U_{\mathrm{ps}} = \frac{9}{8}\rho_{\mathrm{CSM}} v_{\mathrm{sh}}^2$ (the factor of 9/8 in the post-shock thermal energy arises from the Rankine–Hugoniot jump conditions, see discussion in the appendix of L. DeMarchi et al. 2022 for more details) where ρ_{CSM} is the density of the CSM, is transferred to the magnetic field energy density, $U_{\mathrm{B}} = B^2/8\pi$, gives

$$B = \sqrt{9\pi\epsilon_{\mathrm{B}}\rho_{\mathrm{CSM}} v_{\mathrm{sh}}^2}. \quad (5)$$

Therefore, the radial shape of the density profile and the evolution of the shock with time determine the temporal evolution of the magnetic field strength. A typical assumption for the formation of the CSM is via a constant mass-loss rate in steady winds (e.g., stellar winds). This scenario leads to a

[5] Here, we assumed that electron cooling effects are not important at the observed frequency. This is not always the case; see, e.g., SN2020oi (A. Horesh et al. 2020); SN2019oys (I. Sfaradi et al. 2024); SN2012aw (N. Yadav et al. 2014).

density profile of

$$\rho_{\rm CSM}(r) = \frac{\dot{M}/v_{\rm w}}{4\pi r^2}, \quad (6)$$

where $\dot{M}$ is the mass-loss rate and $v_{\rm w}$ is the wind velocity.

External FFA is important when the external optical depth, $\tau_{\rm ff}$, is of the order of unity (as seen in numerous cases, e.g., SN 1979C (K. W. Weiler et al. 1991; SN 2013df (A. Kamble et al. 2016); SN 2019oys (I. Sfaradi et al. 2024); SN 2023ixf (A. J. Nayana et al. 2024)). This will attenuate the flux density shown in Equation (1) by a factor of $e^{-\tau_{\rm ff}}$ where the optical depth of FFA is (see, e.g., A. Horesh et al. 2013c)

$$\tau_{\rm ff} = 0.76\left(\frac{\dot{M}[10^{-6}M_{\odot}\,{\rm yr}^{-1}]}{v_{\rm w}[10\ {\rm km s}^{-1}]}\right)^2\left(\frac{T_{\rm e}}{10^5\ {\rm K}}\right)^{-1.35} \left(\frac{v_{\rm sh}}{10^4\ {\rm km\ s}^{-1}}\right)^{-3}\left(\frac{t}{10\ {\rm days}}\right)^{-3}\left(\frac{\nu}{5\ {\rm GHz}}\right)^{-2.1}, \quad (7)$$

where $T_{\rm e}$ is the temperature of the electrons in the wind.

In the following sections, we analyze the radio data shown in Section 3 in light of the SN–CSM interaction model described above under several assumptions. First, throughout the entire analysis, we assumed that $p = 3$ for stripped-envelope SNe, and $p = 2.4$ for SNe II. This assumption is based on radio observations of the optically thin regime for various CCSNe (see Table 1 in R. A. Chevalier 1998, Table 2 in K. W. Weiler et al. 2002, and the discussion in M. F. Bietenholz et al. 2021). We discuss the implications of changing this assumption in Section 6.2). Another assumption is that of equipartition, and specifically $\epsilon_{\rm e} = \epsilon_{\rm B} = 0.1$. While there is great theoretical and observational motivation for the equipartition assumption (e.g., M. A. Scott & A. C. S. Readhead 1977; R. A. Chevalier 1998; R. Barniol Duran et al. 2013) the exact values of $\epsilon_{\rm e}$ and $\epsilon_{\rm B}$ are not well understood observationally (we discuss the implications of this assumption in Section 6.1). We also assumed that the emission filling factor is $f = 0.5$. This assumption means that the emitting volume is ~20% of the volume engulfed by the shock front. Finally, for the temperature of the CSM we assumed $T_{\rm e} = 10^5$ K but note that the true value for the temperature may vary (see, e.g., P. Lundqvist & C. Fransson 1988; R. A. Chevalier & C. Fransson 2017).

3. Radio SNe Sample

Over the last four decades, astronomers conducted and reported radio observations of CCSNe in different wavelengths (typically in the GHz band) and different timescales after the stellar explosion. We assembled a sample of radio observations of CCSNe using data from literature, online databases, and reports, e.g., The Open SNe Catalogue,[6] ATels,[7] and GCN Circulars.[8] In addition to these previously reported observations, we present here for the first time radio observations of 99 CCSNe conducted with the Arcminute Micro-Kelvin Imager—Large Array (AMI-LA; J. T. L. Zwart et al. 2008; J. Hickish et al. 2018) as part of our systematic observing campaign.

3.1. The AMI-LA

AMI-LA is a radio interferometer comprised of eight, 12.8 m diameter, antennas producing 28 baselines that extend from 18 m up to 110 m in length and operate around a central frequency of 15.5 GHz with a 5 GHz bandwidth, divided into eight channels. For each observation, initial data reduction, flagging, and calibration of the phase and flux, were carried out using `reduce_dc`, a customized AMI-LA data reduction software package (Y. C. Perrott et al. 2013). Phase calibration was conducted using short interleaved observations of the phase calibrator, while daily observations of 3C286 were used for absolute flux calibration. Additional flagging was performed using CASA (J. P. McMullin et al. 2007).

In our observations with the AMI-LA we took a systematic approach. We conducted the first observations as soon as possible (given technical limitations) following a classification of a CCSNe. Then, we aimed to monitor each SN (even in the case of a radio nondetection) on timescales of: a week, a month, three months, half a year, a year, and a year and a half after the explosion. This was done to probe the CSM at different regions around the CCSNe, and in the case of consecutive upper limits, constraining the possible mass-loss rates from the progenitor massive star at different epochs of stellar evolution.

3.2. The Complete Sample

The resulting SNe sample is comprised of 325 SNe, 177 of which are SNe II (including its various subtypes, e.g., II-P, II-L, and IIn; Pec is for peculiar SNe) and 148 are stripped-envelope SNe (Types Ib, Ic, and IIb; BL is for broad-line SNe). Within this set, 72 have radio detections, while 253 have only upper limits on the radio flux density. From this search for radio emission from CCSNe, we find that ~78% of CCSNe in the near universe (90% of the CCSNe in our sample are at a distance of up to 100 Mpc) were not detected in radio wavelengths. See Table 1 for the SNe in our sample and Table 2 in Appendix C for the radio upper limits in our sample. Finally, Table 3 in Appendix C is for the peak flux density of radio-detected SNe (as described in detail in Section 4).

In the following sections, we probe the phase space of density profiles and mass-loss rates from massive stars in light of the model presented in Section 2 using the radio observations of CCSNe in our sample. We first analyze radio-detected SNe and discuss the results in terms of shock velocities and mass-loss rate in Section 4. Next, in Section 5, we use the entire sample of SNe (both radio-detected and radio-nondetected SNe) to probe the CSM density around CCSNe and constrain the phase space of the mass-loss rate from massive stars.

4. Analysis of SNe with Radio Detections

The SN–CSM model described in Section 2 suggests that by observing the radio peak flux density, we can infer the velocity of the shock traveling in the CSM, and the mass-loss rate divided by wind velocity. Thus, in the following section, we analyze SNe (from the sample shown in Section 3) that were detected in radio, by deriving their spectral peak flux density, frequency, and time since the explosion. To accomplish that, we fit the following two power-law spectra to the SN radio data (see Equation (4) in R. A. Chevalier 1998)

$$F_\nu(t) = 1.582\, F_p\left(\frac{t}{t_a}\right)^a\left(\frac{\nu}{\nu_a}\right)^{5/2} \times\left(1 - \exp^{-\left(\frac{t}{t_a}\right)^{-(a+b)}\left(\frac{\nu}{\nu_a}\right)^{-(p+4)/2}}\right), \quad (8)$$

[6] https://sne.space/
[7] http://www.astronomerstelegram.org/
[8] https://gcn.gsfc.nasa.gov/gcn3_archive.html

Table 1
Summary of the Properties of CCSNe in Our Sample

Name	Type	Explosion Date (YYYY/MM/DD)	Distance (Mpc)	Detected (Y/N)	Reference(s)
SN 1979C	II-L	1979/04/06	16.2	Y	K. W. Weiler et al. (1991), M. F. Bietenholz et al. (2021)
SN 1980K	II	1980/10/14	5.5	Y	M. J. Montes et al. (1998), M. F. Bietenholz et al. (2021)
SN 1980O	II	1980/12/30	17.9	N	M. F. Bietenholz et al. (2021)
SN 1981K	II	1981/07/31	7.3	Y	S. D. van Dyk et al. (1992), M. F. Bietenholz et al. (2021)
SN 1982F	II-P	1982/02/24	6.2	N	M. F. Bietenholz et al. (2021)
SN 1986J	II	1983/03/14	10.0	Y	K. W. Weiler et al. (1990), M. F. Bietenholz et al. (2021)
SN 1983N	Ib	1983/06/29	4.9	Y	K. W. Weiler et al. (1986), M. F. Bietenholz et al. (2021)
SN1984E[a]	II-L	1984/03/26	17.54	N	C. R. Eck et al. (1996), M. F. Bietenholz et al. (2021)

Note. In the "Name" column, "[a]" indicates when the discovery date from the open SNe catalog is taken as an explosion date since no other data was available. The distance for these objects is inferred directly from redshift, assuming $H_0 = 70$ km s^{-1}/Mpc and $\Omega_m = 0.25$. Where [a] is not mentioned, the distance and explosion date were taken from the referenced article. All SNe first presented here are marked in the "Reference" column as "This work." For these SNe, the explosion date is based on the discovery date from their TNS page, and their distance is inferred directly from redshift using the same assumption mentioned above. "[b]" indicates when the radio peak is taken directly from the literature and not by the fitting process described in Section 4.

References. L. Dessart et al. (2008), A. Corsi et al. (2010), A. Horesh et al. (2011, 2013b), K. W. Weiler et al. (1991), M. J. Montes et al. (1998), S. D. van Dyk et al. (1992), K. W. Weiler et al. (1986), C. R. Eck et al. (1996), S. D. van Dyk et al. (1998), M. J. Montes et al. (1997), K. W. Weiler et al. (1990), C. L. Williams et al. (2002), S. D. van Dyk et al. (1993), S. D. van Dyk et al. (1996), K. W. Weiler et al. (2007), G. G. Pooley & D. A. Green (1993), K. W. Weiler et al. (2011), P. Chandra et al. (2009), I. Salamanca et al. (2002), C. K. Lacey et al. (1998), D. Pooley et al. (2002a), S. D. Van Dyk et al. (1999), K. W. Weiler et al. (2001), D. Pooley et al. (2002b), C. K. Lacey et al. (1999), P. Chandra et al. (2002), M. A. Pérez-Torres et al. (2009), F. K. Schinzel et al. (2009), C. J. Stockdale et al. (2004a, 2003b), S. D. Ryder et al. (2004), E. Berger et al. (2002), A. M. Soderberg et al. (2005a, 2006a), C. J. Stockdale et al. (2003a), A. Soderberg et al. (2003), R. J. Beswick et al. (2004a), A. J. Nayana et al. (2018), S. Wellons & A. M. Soderberg (2011), K. Misra et al. (2007), C. J. Stockdale et al. (2004b), R. J. Beswick et al. (2004b), A. Elmhamdi et al. (2011), A. M. Soderberg et al. (2004), R. J. Beswick et al. (2005), A. M. Soderberg et al. (2005b), C. J. Stockdale et al. (2005), A. M. Soderberg & S. R. Kulkarni (2005), N. Smith et al. (2017), V. V. Dwarkadas et al. et al. (2016), M. T. Kelley et al. (2006), O. D. Fox et al. (2015), P. Chandra et al. (2007), M. K. Argo et al. (2007), M. Bietenholz & N. Bartel (2007, 2008a, 2008b), S. Chakraborti & A. Ray (2008), P. Chandra et al. (2012), M. Stritzinger et al. (2009), A. M. Soderberg et al. (2010a), P. Chandra & A. Soderberg (2007, 2008), R. Roy et al. (2013), A. J. van der Horst et al. (2011), R. A. Chevalier & A. M. Soderberg (2010), C. J. Stockdale et al. (2008b), C. J. Stockdale et al. (2008e), A. Soderberg et al. (2008), P. Chandra et al. (2008), C. J. Stockdale et al. (2008a), A. Soderberg (2008), C. J. Stockdale et al. (2008d, 2009a), C. J. Stockdale et al. (2008c), C. J. Stockdale et al. (2009b), V. P. Utrobin & N. N. Chugai (2013), P. Chandra & A. Soderberg (2009a), N. Kimani et al. (2016), P. Chandra & A. Soderberg (2009b), A. M. Soderberg et al. (2010b), C. Romero-Cañizales et al. (2014), A. J. van der Horst et al. (2010), C. Romero-Canizales et al. (2011), P. Chandra et al. (2015), M. I. Krauss et al. (2012), A. Horesh et al. (2013c), D. Milisavljevic et al. (2013), S. D. Ryder et al. (2011), S. Chakraborti et al. (2015), A. Kamble et al. (2014), N. Yadav et al. (2014), A. Zauderer et al. (2013), S. Bose et al. (2015), K. Sokolovsky et al. (2013), O. Yaron et al. (2017), M. R. Drout et al. (2016), M. F. Bietenholz et al. (2018), G. E. Anderson et al. (2017), M. Bietenholz & N. Bartel (2014), I. Shivvers et al. (2017), A. J. Nayana & P. Chandra (2018), S. Ryder et al. (2018), S. D. Ryder et al. (2019), I. Sfaradi et al. (2024), A. Horesh et al. (2020), G. P. Srinivasaragavan et al. (2022), K. W. Weiler et al. (2002), M. F. Bietenholz et al. (2021), Y. Cao et al. (2013), A. Horesh et al. (2013a), A. Kamble & A. Soderberg (2013), A. M. Soderberg et al. (2006b).

(This table is available in its entirety in machine-readable form in the online article.)

where ν_a is the frequency where the optical depth is around unity at a time t_a after the explosion, and F_p is the flux density at this time, and a and b are the time evolution power-law indices of the optically thick and thin regimes, respectively. $F_{\nu_a} = 1.582\ F_p$ is the flux density at the intersection between the optically thin and thick regimes (used in the radius and magentic field equations). For a shock wave with a constant expansion velocity traveling in a radial density profile of r^{-2}, we get $a = 2.5$ and $b = 1$ (R. A. Chevalier 1998). When the spectrum of a single SN, at some time t, exhibits both an optically thick and thin regime, we fitted the spectrum with Equation (8) assuming $t = t_a$. F_p, ν_a, and p were treated as free parameters.

For SNe with poor spectral coverage, and a detailed light curve in only one radio frequency, ν, we assumed that a turnover in their radio light curve (if observed) is due to a spectral transition between the optically thick and thin regimes. We treat such SNe by fitting Equation (8) to their radio light curve. The fit free parameters were F_p, t_a, a, and b, and we assumed $\nu = \nu_a$. The results of these fits and the fits of the spectra (with a total of 45 SNe) are summarized in Table 3. In three special cases (SN 2002ap, SN 2008ax, and SN 2012ap), as described in Table 1, we used the spectral peak reported in previous papers.

4.1. Chevalier's Diagram

The phase space of the peak radio luminosity, $L_{\nu_a} = 4\pi D^2 F_{\nu_a}$, and the time of the observation times the observed peak frequency, $t_a\nu_a$, also known as Chevalier's diagram (R. A. Chevalier 1998), is a useful tool to compare radio observations of different CCSNe. By plotting lines of equal shock velocity and mass-loss rates in this phase space, based on Equations (3), (4), (5), and (6), we compare the physical properties of different SNe. In Figure 1, we present all the radio-detected SNe from our sample in a Chevalier diagram (we use different markers to distinguish between the SNe subtypes). For SNe with a limit on the peak flux density, we use an arrow to point in the direction of the limit. Also marked on this plot are lines of equal shock velocities (using Equation (3)), and lines of equal mass-loss rate divided by wind velocity (using Equations (4), (5), and (6)), when assuming constant expansion, $p = 3$, $\epsilon_e = \epsilon_B = 0.1$, and $f = 0.5$. We note here that the analysis of SNe II was done using $p = 2.4$; however, since we wish to present the comparison between stripped-envelope SNe and SNe II we show them on the same plot and choose $p = 3$ for reference.

As seen from this analysis, while the shock velocities of stripped-envelope SNe (filled blue squares for SNe Ib and Ic,

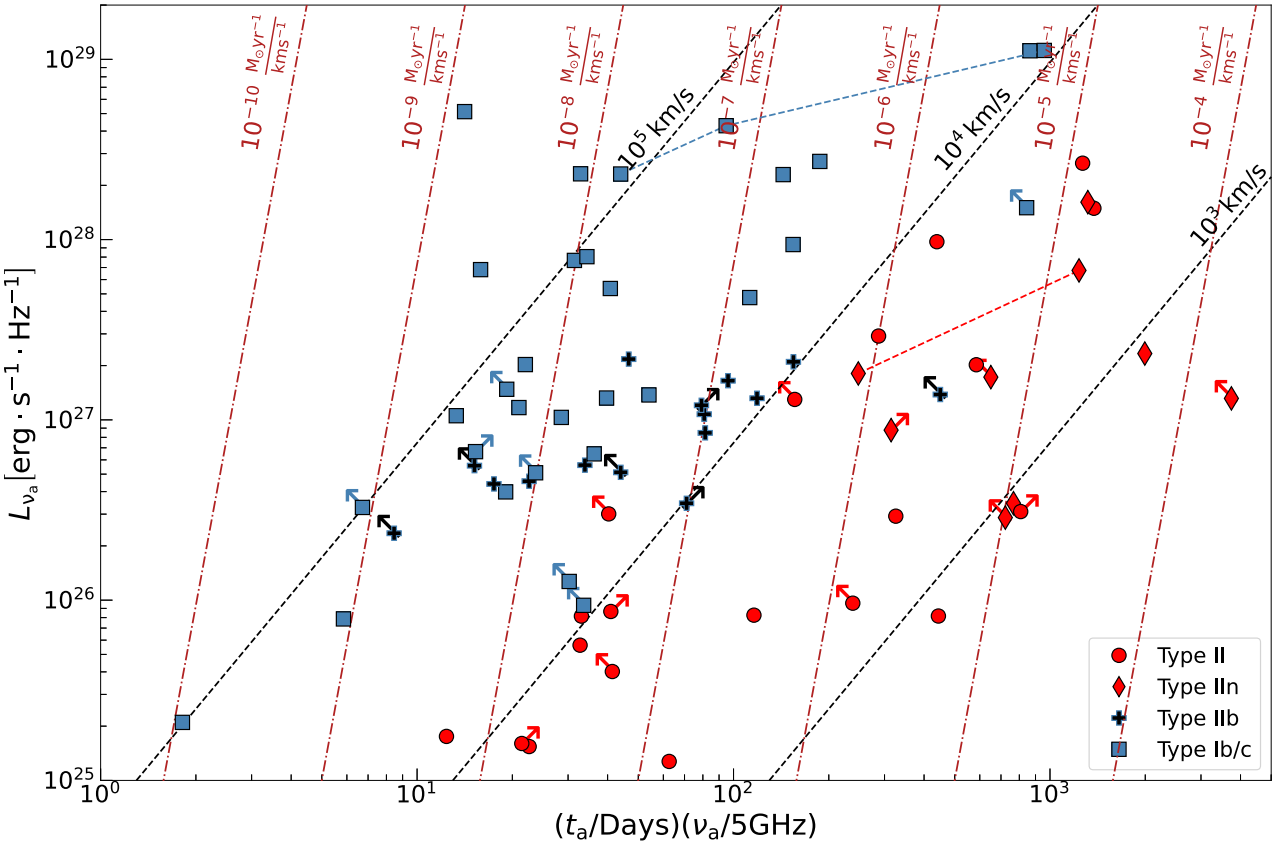

Figure 1. Chevalier diagram showing the peak spectral radio luminosity as a function of $t_a\nu_a$. The peak of each SN was obtained by fitting Equation (4) in R. A. Chevalier (1998) to the spectrum at a specific time, or to the light curve of a specific frequency (see Section 4). The arrows are for an SN whose peak was not observed, and the direction of the arrow indicates whether the peak is in later or earlier times than the time of the highest observed flux density. Points connected with dashed lines represent multiple peaks in the radio light curves for a single SNe. Lines of equal shock velocity (dashed black lines), and of the CSM density parameter (dashed–dotted red lines) are plotted according to Equations (3), (4), (5), and (6) under the assumption that the peak is due to SSA, and of $p = 3$, $f = 0.5$ and equipartition ($\epsilon_e = \epsilon_B = 0.1$). Although we derive the mass-loss rate for SNe II assuming $p = 2.4$, for the sake of comparison only, and specifically for this Chevalier diagram, we present the lines of equal shock velocities and mass-loss rates assuming $p = 3$.

and black plus signs for SNe IIb) are $\geqslant 10^4$ km s^{-1} and their median is ~3×10^4 km s^{-1} (excluding SNe that are associated with relativistic outflows as discussed in Section 4.2), SNe II (filled red circles for regular SNe II and filled red diamonds for SNe IIn) experience significantly slower shocks. The median of SNe II shock velocities is ~5000 km s^{-1} with the fastest being ~1.1×10^4 km s^{-1}. At first sight, the SN–CSM shock velocities measured for some SNe II in our sample may conflict with the photospheric optical velocities, which tend to be around 10^4 km s^{-1} for SNe II. However, some of the SN–CSM shock velocities measured via our radio analysis may represent a late-time velocity, obtained much later after the optical data was obtained, mostly at times >400 days after the explosion, and when the ejecta may have decelerated. We also note that FFA can affect the radio emission of some SNe II with high mass-loss rates and slow wind velocities. In these cases, as the peak frequency and flux density do not depend only on SSA, the mass-loss rate we derived based on this SSA analysis will become lower limits. (K. W. Weiler et al. 2002; R. A. Chevalier & C. Fransson 2017; M. F. Bietenholz et al. 2021). We also note here that in the case of a power-law evolution of the radius with time, $R \sim t^m$ ($m \leqslant 1$ for a nonaccelerating shock wave), the true shock velocity is smaller, $v_{sh} = mR/t$. As explained in Section 5, to avoid complicating the analysis by introducing an unknown power-law index, m, we limit our analysis of radio upper limits to observations made in the first 18 months after the explosion and assume that the shock has not decelerated significantly during this time (i.e., $m = 1$).

Examining the mass-loss rate divided by the wind velocity parameter of these radio-detected SNe shows that SNe II (excluding Type IIn) exhibit $4 \times 10^{-9} < \frac{\dot{M}[M_\odot\ \mathrm{yr}^{-1}]}{v_w[\mathrm{km\ s}^{-1}]} < 10^{-5}$) with a median of $\dot{M}/v_w \sim 10^{-6}\ \frac{M_\odot\ \mathrm{yr}^{-1}}{\mathrm{km\ s}^{-1}}$. If, instead, the absorption mechanism is purely FFA, using Equation (7) and an assumed shock velocity of 10,000 km s^{-1} will increase the median and inferred minimum and maximum mass-loss rate values by about an order of magnitude. Stripped-envelope SNe, on the other hand, exhibit $10^{-10} < \frac{\dot{M}[M_\odot\ \mathrm{yr}^{-1}]}{v_w[\mathrm{km\ s}^{-1}]} < 5 \times 10^{-6}$ with a median of $\dot{M}/v_w = 2 \times 10^{-8}\ \frac{M_\odot\ \mathrm{yr}^{-1}}{\mathrm{km\ s}^{-1}}$.

The CSM densities we derived for SNe II and stripped-envelope SNe are in agreement with the values suggested by stellar evolution models and observational prescription for mass-loss rates (N. Smith 2014). For example, the progenitors of SNe II-P exhibit mass-loss rates of 10^{-6}–$10^{-5}\ M_\odot\ \mathrm{yr}^{-1}$ with wind velocities of 10–20 km s^{-1}, and those of SNe II-L are expected to exhibit mass-loss rates of 10^{-5}–$10^{-4}\ M_\odot\ \mathrm{yr}^{-1}$ with wind velocities of 20–40 km s^{-1}. This results in a range of $\dot{M}/v_w = 5 \times 10^{-8} - 5 \times 10^{-5}\ \frac{M_\odot\ \mathrm{yr}^{-1}}{\mathrm{km\ s}^{-1}}$, which is in agreement with the high values we infer for SNe II. He stars and

Wolf–Rayet stars, which are the suggested progenitors of SNe Ib and Ic, exhibit mass-loss rates of 10^{-7}–$10^{-4}\,M_{\odot}\,\mathrm{yr}^{-1}$ wind winds of $1000\,\mathrm{km\,s}^{-1}$ (which translates to $10^{-10} < \frac{\dot{M}[M_{\odot}\,\mathrm{yr}^{-1}]}{v_{\mathrm{w}}[\mathrm{km\,s}^{-1}]} < 10^{-7}$). This covers, together with the proposed progenitor of SNe IIb (with mass-loss rates of 10^{-5}–$10^{-4}\,M_{\odot}\,\mathrm{yr}^{-1}$ wind winds of 20–100 $\mathrm{km\,s}^{-1}$, which translates to $10^{-7} < \frac{\dot{M}[M_{\odot}\,\mathrm{yr}^{-1}]}{v_{\mathrm{w}}[\mathrm{km\,s}^{-1}]} < 5\times10^{-5}$), the entire range we find for stripped-envelope SNe.

This analysis also reflects the high mass-loss rates, of >few $\times\,10^{-3}\,M_{\odot}\,\mathrm{yr}^{-1}$ (for wind velocity of $10\,\mathrm{km\,s}^{-1}$), from the progenitors of SNe IIn. This matches the interpretation of their optical spectra in which the observed strong and narrow emission lines are assumed to be a result of interaction with highly dense CSM. These high densities correspond to high mass-loss rates that are not easily explained by mass loss in stellar winds and may result from short-lived, episodic, mass-loss processes. Episodic mass-loss processes might occur in close binary interaction or eruptions of luminous blue variables and the most extreme cool hyper-giants. These are the only classes of stars with observed high wind densities that can form the narrow lines (see the discussions in N. Smith 2017 and P. Chandra 2018, and the possible progenitors of, e.g., SN 2010jl (N. Smith et al. 2011) and SN 2005gl (A. Gal-Yam et al. 2007)).

4.2. Treating Special Cases in Further Analysis

The analysis presented above showed some SNe that their observational and physical properties deviate from our model assumptions (e.g., relativistic velocities, shock deceleration, and multi-peaked light curves). We briefly discuss these special cases here:

1. *SN 1998bw, SN 2002ap, SN 2009bb, and SN 2012ap.* These SNe are associated with relativistic ejecta and thus need to be treated differently (SN 1998bw (K. W. Weiler et al. 2001); SN 2002ap (E. Berger et al. 2002); SN 2009bb (A. M. Soderberg et al. 2010b), and SN 2012ap (S. Chakraborti et al. 2015)). They are shown in Figure 1 only for reference, and we exclude these SNe in further analysis.
2. *SN 2014C and SN 2007bg.* Exhibit several peaks in their radio light curve. This suggests that the SN ejecta interacts with multiple CSM shells deposited in separate mass-loss stages. Since the mass-loss history of these SNe clearly diverts from the scenario of constant mass loss in steady winds, we do not use SN 2014C and SN 2007bg in our analysis.
3. *SNe IIn.* Show narrow optical lines that are associated with the interaction of the ejecta with a dense CSM, which is not in agreement with the scenario of constant mass loss by steady winds. This results in a different radio evolution than seen in regular Type II (including II-L and II-P) and is therefore marked as a different group. Due to their nontypical radio evolution and mass-loss processes, in the following analysis, we exclude all SNe IIn.

After removing these 16 cases, when further analyzing radio-detected SNe, we are left with 18 SNe II and 38 stripped-envelope SNe. Out of these radio-detected SNe, the radio spectral peak of six SNe II and 12 stripped-envelope SNe was not observed, and only a lower limit on the peak flux density was given. Therefore, we have an observed peak for 12 SNe II and 26 stripped-envelope SNe.

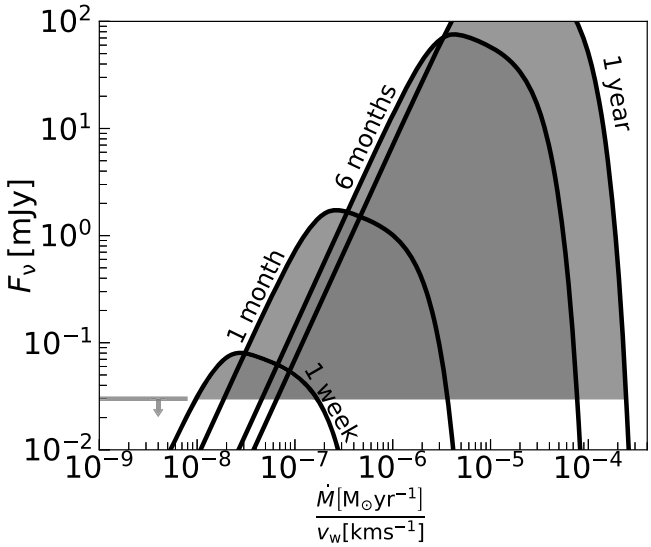

Figure 2. The radio flux density (at 15.5 GHz) as a function of $\dot{M}/v_{\mathrm{w}}$ under the SN–CSM interaction model presented in Section 2 at different timescales (a week, a month, 6 months, and a year) after the SN explosion. A 3σ upper limit of 0.03 mJy (plotted on the bottom left) is translated to ruled-out regions in $\dot{M}/v_{\mathrm{w}}$ as all values of $\dot{M}/v_{\mathrm{w}}$ that produce higher flux densities than the upper limit are ruled out (this is seen in the shaded areas). Here, we assumed synchrotron emission from an SN at a distance of 20 Mpc, shock velocity of $10^{4}\,\mathrm{km\,s}^{-1}$, $\epsilon_{\mathrm{e}} = \epsilon_{\mathrm{B}} = 0.1$, $p = 3$, and $f = 0.5$, and a temperature of the electrons of 10^{5} K.

5. Constraining the CSM Density Phase Space

We now aim to probe the phase space of CSM density around massive stars (and the resulting mass-loss rates) using the full CCSNe sample presented in Section 3 (radio-detected and nondetected SNe; see a plot of all the radio upper limits in our sample in Figure 3) under the same model presented in Section 2.

For a given SN with a flux density upper limit, F_{ν}, taken at a frequency, ν, Equation (1) (multiplied by $e^{-\tau_{\mathrm{ff}}}$ to account for FFA) provides limits on the possible magnetic fields if we assume a radius for the emitting shell. This radius can be calculated under the assumption of a typical shock velocity,[9] v_{sh}, and of constant expansion, $R = v_{\mathrm{sh}}\Delta t$, where Δt is the time of the observation since the SN explosion. Thus, every SN radio upper limit rules out a region in the CSM density phase space (using the relation in Equation (5) between the magnetic field strength and the density). These ruled-out regions in the phase space of ρ_{CSM} are translated to ruled-out regions in the phase space of $\dot{M}/v_{\mathrm{w}}$ using Equation (6). In Figure 2 we show an example of how upper limits on the radio emission are translated to ruled-out regions in $\dot{M}/v_{\mathrm{w}}$ phase space, ruled-out regions in ρ_{CSM} are derived similarly.

In Figure 4 we present the results of applying this analysis to the entire CCSNe sample.[10] As seen from this analysis, we managed to probe the density around massive stars to the extent of ~10^{15}–10^{17} cm. For SNe II, this translates to mass loss at the last ~10–2000 yr of stellar evolution (assuming wind velocity

[9] In the following analysis, we assume shock velocities of $10^{4}\,\mathrm{km\,s}^{-1}$ for SNe II and $3\times10^{4}\,\mathrm{km\,s}^{-1}$ for stripped-envelope SNe, similar to the velocities inferred for radio-detected SNe in Section 4.

[10] We note here that we limit our analysis to flux density upper limits obtained up to a year and a half after the explosion. This is due to the possible shock deceleration at late times. Therefore, when analyzing nondetected SNe, we are left with a total of 148 out of 226 (not including the removal of the SNe IIn mentioned in Section 4.2).

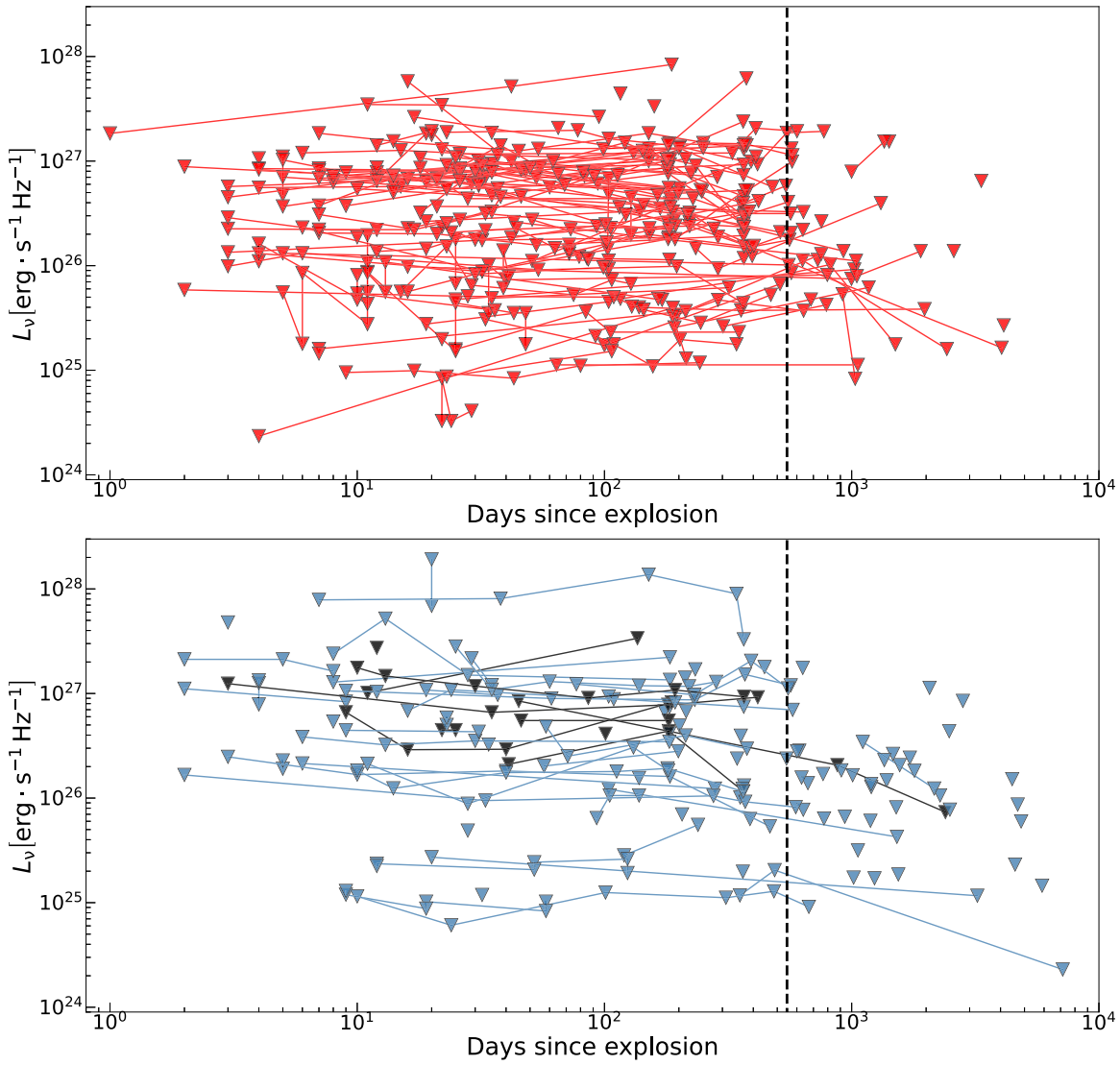

Figure 3. Limits on the specific radio luminosity from the SNe in our sample that were not detected in radio wavelengths. Each limit is marked with a triangle, and the lines are connection limits from the same SN. The top panel shows the limits on the radio emission from SNe II SNe (excluding Type IIn as discussed in Section 4.2). The bottom panel shows the limits on the radio emission from stripped-envelope SNe (blue is for SNe Ib/Ic, and black is for SNe IIb). Also marked for reference (in a vertical dashed line) is the year-and-a-half timescale as we limit our analysis to flux density upper limits obtained up to a year and a half after the explosion. This is due to the possible shock deceleration at late times, as seen in some SNe II in Section 4.

of 10 km s^{-1}), and the last few months up to 1000 yr of stellar evolution for stripped-envelope SNe. Our systematic observations with AMI-LA play a key role here by ruling out mass-loss rates over the extent of thousands of years before the explosion. According to Figure 4, for the progenitors of at least 25% of the SNe II in our sample, we rule out mass-loss rates in the range of 2×10^{-7}–$10^{-4}\,M_\odot\,\mathrm{yr}^{-1}$ (assuming wind velocity of 10 km s^{-1}). For the progenitors of at least 20% of the stripped-envelope SNe in our sample (as suggested by Figure 4), we rule out mass-loss rates $\gtrsim 5 \times 10^{-5}\,M_\odot\,\mathrm{yr}^{-1}$ (assuming wind velocity of 1000 km s^{-1}).

While it is useful to probe the ruled-out density profiles seen in Figure 4, another way to look at these limits is by probing the ruled-out regions in the phase space of mass-loss rate divided by wind velocity. Since each SN might have several limits, stacking them will give a range of ruled-out $\dot{M}/v_\mathrm{w}$ for each SN. Here, we assumed that the CSM was deposited via constant mass loss in steady winds throughout the entire evolution of the progenitor star. We show this analysis in Figure 5 (In Figure 8 in Appendix A, we show the same results for typical wind velocities), and a comparison in percentages in Figure 6. As suggested in the left panels of these figures, assuming $v_\mathrm{w} = 10$ km s^{-1}, for 82% (87 out of 106) of the SNe II with limits on their mass-loss rate, the region of mass-loss rate between 2×10^{-6} and $10^{-4}\,M_\odot\,\mathrm{yr}^{-1}$ is ruled out. Values of mass-loss rates in that range are inferred for 67% (eight out of 12) of the SNe with an observed peak in the radio. In the case of stripped-envelope SNe (right panels of Figures 5 and 6), assuming $v_\mathrm{w} = 1000$ km s^{-1} suggests that ~86% (62 out of 72) of the SNe with limits on their mass-loss rate rules out the region of 5×10^{-5}–$5 \times 10^{-3}\,M_\odot\,\mathrm{yr}^{-1}$. A value of mass-loss rate in this region is inferred for ~40% (11 out of 26) of the stripped-envelope SNe with an observed radio peak.

This analysis points to a discrepancy between the values of $\dot{M}/v_\mathrm{w}$ inferred from radio-detected SNe and radio-nondetected SNe, especially for the case of SNe II. Thus, detecting SNe in radio wavelengths is highly biased toward progenitor stars that experience high mass-loss rates at their last stages of stellar evolution. As noted above, if we change our assumption to

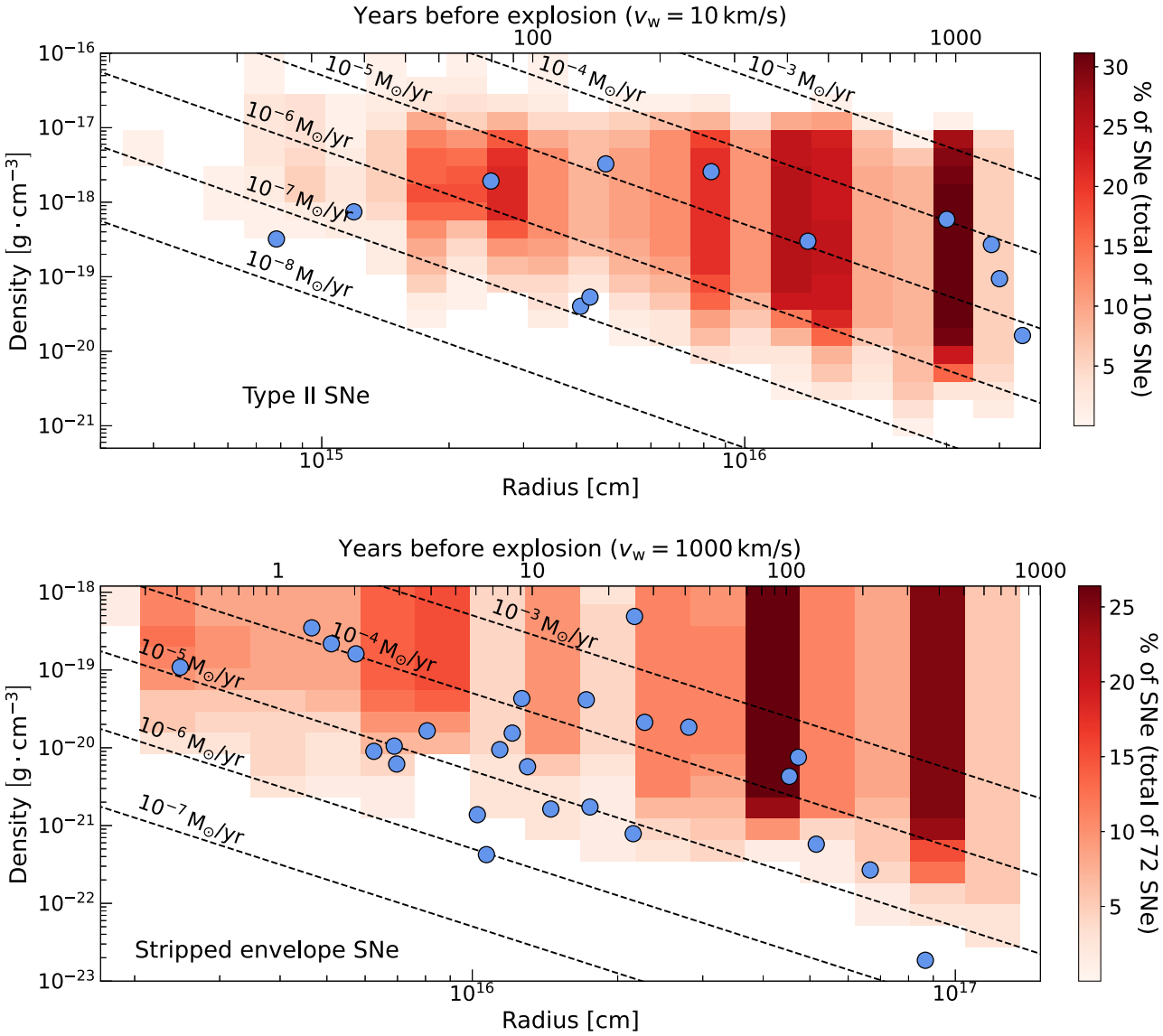

Figure 4. These plots summarize the ruled-out regions in phase space of the density profile around the CCSNe in our sample. The color map shows the percentage of SNe II (top panel) and stripped-envelope (bottom panel) SNe in our sample that rule out a density for a given radius (both SNe that were not detected in radio wavelengths at all, and SNe with limits on their peak flux density). Here, we assumed a constant shock velocity of 10,000 km s^{-1} for SNe II, and 30,000 km s^{-1} for stripped-envelope SNe. The blue markers are of the measured densities from SNe in which the peak of their radio light curve or spectra is observed.

include FFA as the dominant absorption mechanism for SNe II with an observed radio peak, the range of mass-loss rate values will increase by about an order of magnitude. However, the discrepancy between radio-detected and radio-nondetected SNe still remains. If the peak of the radio emission of SNe II is dominated by FFA, the range of ~10^{-7} and ~$3 \times 10^{-4}\,M_\odot\,\mathrm{yr}^{-1}$ is inferred for 67% of the SNe with an observed radio peak (for an assumed $v_w = 10\,\mathrm{km\,s}^{-1}$). This range is ruled out by 70% of the SNe with limits on their radio emission.

Theoretical and observational mass-loss prescriptions predict a range of possible mass-loss rates and wind velocities (N. Smith 2014). A large fraction of these regions are ruled out by large fractions of radio-nondetected SNe II. For example, the suggested range of $\dot{M}/v_w$ for the likely progenitors of SNe II-P (RSG) is $5 \times 10^{-8} \leqslant \frac{\dot{M}\,[M_\odot\,\mathrm{yr}^{-1}]}{v_w\,[\mathrm{km\,s}^{-1}]} \leqslant 10^{-6}$. It has also been suggested that the likely progenitors of SNe II-L (RSG/YSG) experience a mass-loss rate to wind velocity ratio between 2.5×10^{-7} and $5 \times 10^{-5}\,\frac{M_\odot\,\mathrm{yr}^{-1}}{\mathrm{km\,s}^{-1}}$. However, we find that the entire range suggested for the progenitors of SNe II-L and II-P is being ruled out by 30% and 50%, respectively, of the SNe II in our sample that only have limits on their mass-loss rates. High values of mass-loss rates ($\gtrsim$few $\times\ 10^{-3}\,M_\odot\,\mathrm{yr}^{-1}$ with winds of $10\,\mathrm{km\,s}^{-1}$) cannot be ruled out in this analysis as FFA plays an important role in such cases, especially at early times. However, SNe with such high mass-loss rates (and resulting high densities) should exhibit narrow emission lines in their optical spectrum. We note that we excluded SNe IIn from our analysis, although we do not have full optical spectral cover for all SNe in our sample.

In this work we provide multi-epoch systematic monitoring on a logarithmic scale of a large sample CCSNe. Systematic monitoring at this scale has never been done before, and these results emphasize the importance of systematic observations and continuous follow-up even when a target is not detected. We also note that while the ranges of mass-loss rates we infer are not different from previous works, in this work, we take a different approach in our analysis. Past studies often focused on the mass-loss rates from small samples of radio-detected SNe

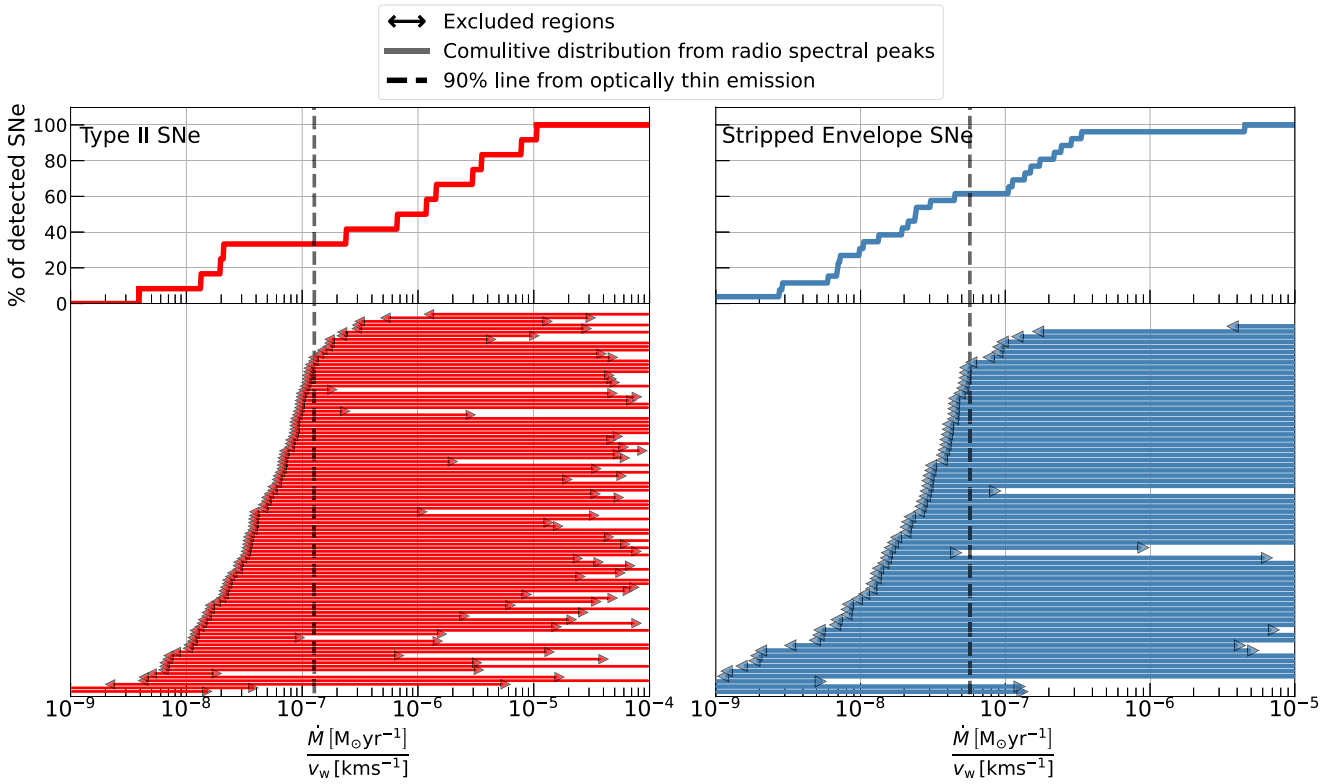

Figure 5. Representation of the phase space of mass-loss rate divided by wind velocity using combined data from both radio-detected and radio-nondetected SNe. This plot shows the ruled-out regions as limits on $\dot{M}/v_w$ (as described in Section 5), and the distribution of this parameter as obtained from a peak in the radio light curve or spectra of radio-detected SNe (as described in section 4). The left panel shows the results for SNe II, while the right panel is for stripped-envelope SNe. Shock velocities of 10^4 km s^{-1} are assumed for SNe II, while for stripped-envelope SNe, we assumed 3×10^4 km s^{-1}. In this plot, there are 56 radio-detected (18 SNe II and 38 stripped-envelope SNe) and 160 radio-nondetected SNe (100 SNe II and 60 stripped-envelope SNe). The radio peak has been observed for 38 of them (12 SNe II and 26 stripped-envelope SNe) and is represented in the histograms, and for 18, we only have limits on their spectral peak, represented in the ruled-out regions. Also plotted for reference are the lines that correspond to the 90% of the SNe with limits on the CSM phase space, which rule out values of $\dot{M}/v_w$ greater than it. In Figure 8 in Appendix A, we show the same results for typical wind velocities, i.e., the phase space of mass-loss rate (not divided by wind velocity).

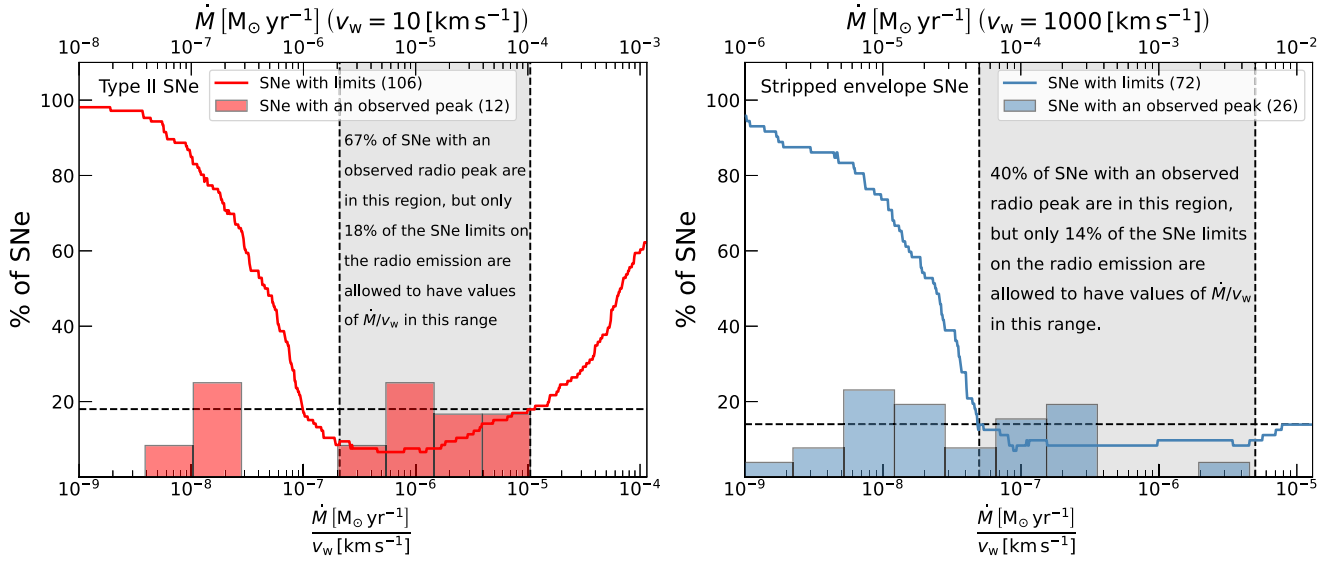

Figure 6. Comparison of mass-loss history between SNe with an observed radio peak, and SNe with radio limits. For the SNe with an observed radio peak, we present the distribution of $\dot{M}/v_w$ (bar histogram). For the SNe with limits on their radio emission, or on their radio peak, we present the percentages of SNe that are allowed for each value of $\dot{M}/v_w$ (step diagram). The left panel shows the results for SNe II and the right panel is for stripped-envelope SNe. Also marked in shaded regions is the area in the phase space of $\dot{M}/v_w$ that shows the discrepancy between the values inferred from SNe with radio peaks and SNe with limits. We also evaluate this phase space for mass-loss rates assuming typical wind velocities (top x-axes).

(R. A. Chevalier 1998; K. W. Weiler et al. 2002), very late-time observations (years after the explosion) corresponding to earlier epochs of stellar evolution compared to the SN explosion (K. Rose et al. 2024), and average values and width of the distributions of mass-loss rates based on a large sample of radio-detected and nondetected CCSNe (M. F. Bietenholz et al. 2021).

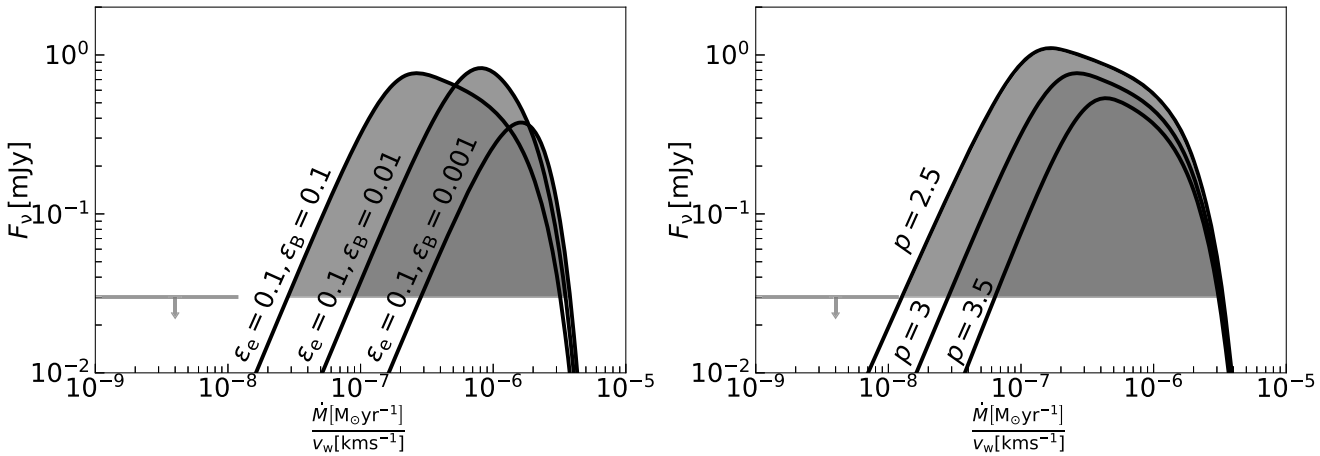

Figure 7. The radio flux density (at 15.5 GHz) as a function of $\dot{M}/v_w$ under the SN–CSM interaction model presented in Section 2 at 30 days after the SN explosion. A 3σ upper limit of 0.03 mJy (plotted on the bottom left) is translated to ruled-out regions in $\dot{M}/v_w$ as all values of $\dot{M}/v_w$ that produce flux density higher than the upper limit are ruled out (this is visible through the shaded areas). Here, we assumed synchrotron emission from an SN at a distance of 30 Mpc, and shock velocity of 10^4 km s^{-1}. In the left panel. we assume $\epsilon_e = 0.1$, $p = 3$, $T_e = 10^5$ K, and $f = 0.5$, while varying ϵ_B. In the right panel, we assume $\epsilon_e = \epsilon_B = 0.1$, $T_e = 10^5$ K, and $f = 0.5$, while varying p.

We, on the other hand, use our sample to probe the phase space of mass-loss rate and to compare the distribution of mass-loss rates inferred from radio-detected SNe to the ruled-out regions due to radio upper limits. This comparison leads to the conclusion that there is a large discrepancy between the progenitors of radio-detected and nondetected SN regarding mass loss during their final stages of evolution.

6. Testing Model Assumptions

The analysis presented above, both when we had radio detections (Section 4), and when we had only radio upper limits (Section 5), was performed under several simplifying assumptions. Changing our assumptions, such as the electron energy power-law index, p, and energy equipartition ($\epsilon_e = \epsilon_B = 0.1$), will change the derived mass-loss rate. In the following section, we test how varying these assumptions will impact our conclusions on the mass-loss rate phase space.

6.1. Deviation from Equipartition

Deviations from equipartition have been observed for a handful of SNe (mostly stripped-envelope SNe, e.g., SN 2011dh (A. M. Soderberg et al. 2012; A. Horesh et al. 2013c) SN 2012aw (N. Yadav et al. 2014); SN 2020oi (A. Horesh et al. 2020)), which all point toward $f_{eB} > 1$. A typical assumption is that $\epsilon_e = 0.1$. Thus, we now discuss deviations where $\epsilon_e = 0.1 > \epsilon_B$.

As seen from Equation (3), the derivation of the radius of the emitting shell from the radio spectral peak goes as $f_{eB}^{-1/19}$, and therefore, so does the shock velocity (assuming free expansion). For $f_{eB} = 10$, the inferred shock velocity will be reduced by ~11%, and for $f_{eB} = 100$, by ~23%. The magnetic field strength (derived from the radio spectral peak; Equation (4)) scales as $f_{eB}^{-4/19}$ and therefore will be reduced by 38% and 62 for $f_{eB} = 10$ and 100, respectively. Overall, changing f_{eB} from 1 to 10 and 100 (assuming $\epsilon_e = 0.1$) will increase the mass-loss rate by a factor of 3.8 and 14, respectively.

A flux density upper limit will result in a weaker upper limit on the mass-loss rate due to deviation from equipartition (mainly by decreasing ϵ_B, see the top-right panel of Figure 7). Therefore, radio nondetection of nonequipartition shock waves traveling in a CSM will be less constraining on the low end of the mass-loss rate parameter space (for reference, we show the results of this analysis assuming $\epsilon_e = 0.1$ and $\epsilon_B = 0.01$ in Appendix B).

6.2. Electron Energy Power-law Index

Throughout our analysis, we assumed that the accelerated electrons in the shock front gain energy density distribution of E^{-p} with $p = 3$ for stripped-envelope SNe and $p = 2.4$ for SNe II. While this is a reasonable assumption, different values of optically thin power-law indices have been observed implying that the values of p are sometimes lower or higher than these values (see Table 1 in R. A. Chevalier 1998 and Table 2 in K. W. Weiler et al. 2002 for different power-law indices for the energy distribution of the electrons). Testing the effect of $\Delta p = \pm 0.5$ shows that the shock velocity and the $\dot{M}/v_w$ measured from a radio spectral peak (assuming SSA) will change by 17% and 50%, respectively. We also test the effect on the phase space of ruled-out $\dot{M}/v_w$ from radio-nondetected SNe by changing p. The bottom panel of Figure 7 shows the radio flux density from an SN as a function of the CSM density parameter for different values of p. A flux density upper limit will rule out smaller regions in the mass-loss rate phase space if we assume $p > 3$, and larger regions if we assume $p < 3$ (for reference, we show the results of this analysis for SNe II assuming $p = 2.1$ and 3 in Appendix B).

7. Summary and Conclusions

In this work, we analyzed radio observations of CCSNe from a population point of view. We form a sample of more than 300 CCSNe with radio observations, comprised of both archival and new (first presented here) observations. We find that while it is not rare to detect them in radio wavelengths, the majority of CCSNe, about 78%, are not detected in radio wavelengths even when monitored over a large range of timescales. We analyzed the entire sample using the SN–CSM interaction model and probed the resulting phase spaces of CSM density around CCSNe and mass-loss rate from the progenitor massive stars.

Our analysis suggests that most SNe have different values of CSM density around them than what is suggested by only analyzing SNe in which a peak in their radio light curve or spectra

is observed. This means that the majority of SNe experience different values of mass-loss rate than typically reported. For example, while ~70% of the SNe II with an observed peak in the light curve or spectrum experience $2 \times 10^{-6} \leqslant \frac{\dot{M}}{M_{\odot}\ \mathrm{yr}^{-1}} \leqslant 10^{-4}$ for an assumed wind of 10 km s^{-1}, the vast majority of the other subset of SNe II (about ~80%) rule out this range of mass-loss rates. For stripped-envelope SNe, on the other hand, 40% of the SNe with an observed peak in their radio light curve or spectra experience $5 \times 10^{-5} \leqslant \frac{\dot{M}}{M_{\odot}\ \mathrm{yr}^{-1}} \leqslant 5 \times 10^{-3}$ for an assumed wind of 1000 km s^{-1}. However, 86% of the stripped-envelope SNe with limits on their mass-loss rate point to $\dot{M} \leqslant 5 \times 10^{-5}\, M_{\odot}\ \mathrm{yr}^{-1}$.

Red supergiants (RSGs) are the likely progenitors of SNe II-P and II-L, which are the majority of SNe II in our sample. These progenitors can experience mass-loss rates between 10^{-6} and $10^{-5}\,\mathrm{M}_{\odot}\,\mathrm{yr}^{-1}$ and wind velocities as high as 40 kms^{-1} (N. Smith 2014). The low end of this range can explain some of the SNe II that rule out values $\leqslant 4 \times 10^{-6}\, M_{\odot}\ \mathrm{yr}^{-1}$ but there is still a substantial fraction of them that cannot be explained by these models. Furthermore, various stellar evolution models and observations suggest a range of possible mass-loss rates. However, most of it (namely $10^{-6} < \dot{M} < 10^{-4}\, M_{\odot}\ \mathrm{yr}^{-1}$ for winds of 10 km s^{-1}) is ruled out by the majority of Type II SNe in our sample.

While the assumption of constant mass-loss rate in steady winds plays a key role in our analysis and conclusions of the phase space of mass-loss rates from massive stars, there are examples of clear deviation from such a simple scenario (see, e.g., SN 2003L (A. M. Soderberg et al. 2005a); SN 2014C (G. E. Anderson et al. 2017); SN 2004c (L. DeMarchi et al. 2022); SN 2019oys (I. Sfaradi et al. 2024)), and other mass-loss mechanisms can take place (e.g., binary stars interactions and violent mass ejections). We emphasize here that this work takes a step forward in constraining the wind model from a statistical point of view. Any future work combining the systematic approach taken here with deeper limits and even more epochs, constraining even larger radii around the SN and shorter timescales compared to the time since the explosion, can shift our understanding of the mass-loss mechanisms that shape massive stars at the end of their lives and possibly determine the role of winds in the last thousand years of evolution.

Our systematic approach of probing newly reported CCSNe on different timescales after the SN explosion has proven to be valuable. The analysis above amplifies the importance of systematically observing CCSNe in radio wavelengths. More sensitive observations with state-of-the-art facilities (such as the Karl G. Jansky Very Large Array) can improve our understanding of the last stages of stellar evolution by probing the phase space of mass-loss rates to lower values (with early observations) and to higher values (with late-time observations). Furthermore, high cadence observations (on timescales of days) can probe variable mass loss on timescales of only a few years before the SN explosion.

Acknowledgments

A.H. is grateful for the support of the Israel Science Foundation (ISF grant 1679/23) and the United States-Israel Binational Science Foundation (BSF grant 2020203). A.H. is supported by the Sir Zelman Cowen Universities Fund. We acknowledge the staff who operate and run the AMI-LA telescope at Lord's Bridge, Cambridge, for the AMI-LA radio data. AMI-LA is supported by the Universities of Cambridge and Oxford, and by the European Research Council under grant ERC-2012-StG-307215 LODESTONE.

Appendix A
Different Wind Velocities

Our analysis in Section 5 shows the results of the mass-loss rate divided by wind velocity ($\dot{M}/v_{\mathrm{w}}$) phase space. However, it is useful to show these results in the context of mass-loss rate under typical wind velocities. In Figure 8 we present the phase space of mass-loss rate under wind velocities of 10, 50, and 100 km s^{-1} for SNe II (top-left, top-right, and bottom-left panels), and 1000 km s^{-1} for stripped-envelope SNe (bottom-right panel).

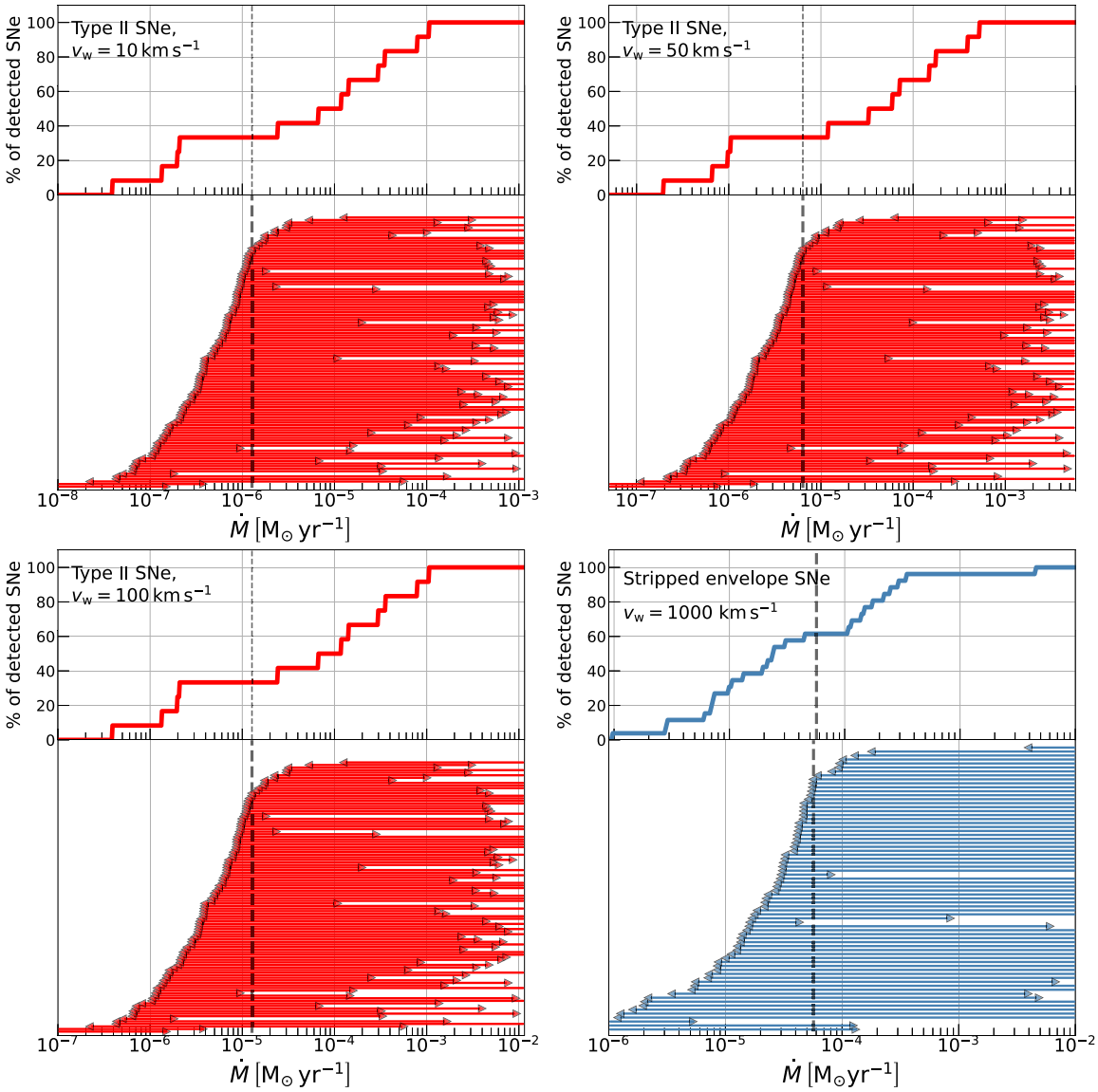

Figure 8. Representation of the phase space of mass-loss rate for different wind velocities using combined data from both radio-detected and radio-nondetected SNe. These plots are similar to the plots seen in Figure 5 but the values of $\dot{M}/v_w$ are multiplied by typical wind velocities. For SNe II, we show the results for $v_w = 10$ km s^{-1} (top left), 50 km s^{-1} (top right), and 100 km s^{-1} (bottom left). For stripped-envelope SNe, we show the results for $v_w = 1000$ km s^{-1} (bottom right).

Appendix B
Different Model Parameters

In Section 6, we discussed the effects of changing the microphysical parameters of the shock on the inferred mass-loss rates. Below, we present the phase space of $\dot{M}/v_w$ when assuming different values of the electron power-law index, p, and the fraction of energy that goes into the magnetic fields, ϵ_B (see Figure 9). The total effect of reducing ϵ_B by an order of magnitude (top-right panel) compared to the original set of assumptions ($p = 3$ for stripped-envelope SNe, $p = 2.4$ for SNe II, and $\epsilon_B = 0.1$) is shifting $\dot{M}/v_w$ to higher values. This does not change our conclusion of the discrepancy between radio-nondetected SNe and SNe with an observed peak; however, the ruled-out region of $\dot{M}/v_w$ does not rule low values suggested by theoretical models (as discussed in Section 7 for the progenitors of SNe II-P and II-L). As seen from the two bottom plots, setting $p = 2.1$ (bottom-left plot) shifts the entire phase space to lower values, i.e., we rule out lower values of $\dot{M}/v_w$, while increasing p to 3 shifts the entire phase space to higher values of $\dot{M}/v_w$. This implies that low values of the electron power-law index rule out even lower values of $\dot{M}/v_w$, deepening the disagreement with mass-loss rates inferred from standard stellar evolution models (N. Smith 2014). On the other hand, higher values of p do not rule low values suggested by theoretical models (as was seen for ϵ_B and discussed in Section 7 for the progenitors of SNe II-P and II-L).

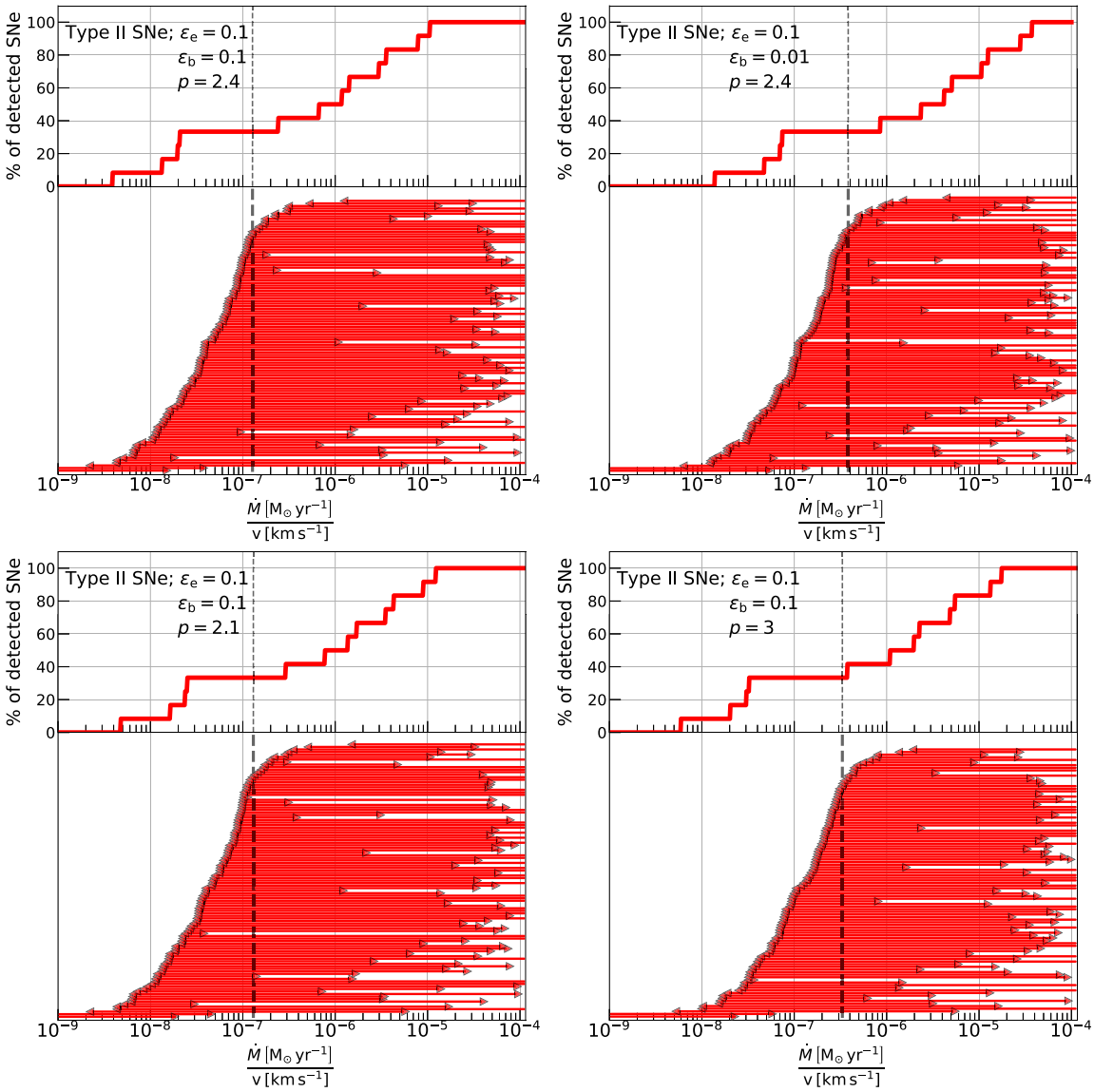

Figure 9. Representation of the phase space of mass-loss rate for different assumptions on the microphysical parameters. These plots are similar to the plots seen in Figure 5 but the values of p and ϵ_B are varied to show the effect of changing our model assumptions. In the top-left panel, we show the results with the same assumptions made in this paper. In the top-right panel, we assume $p = 2.4$ and $\epsilon_B = 0.01$. In the two bottom panels, we assume $\epsilon_B = 0.1$ and $p = 2.1$ (left panel), and $p = 3$ (right panel).

Appendix C
Data Tables

Table 2 provides a summary of the radio upper limits for nondetected SNe. Table 3 provides a summary of the peak flux densities of radio-detected SNe. Each table is published in its entirety in the machine-readable format in the online Journal.

Table 2
Radio Upper Limits of CCSNe

Name	Δt (days)	ν (GHz)	F_ν (mJy)
SN 1980O	2589	4.86	<0.36
SN 1982F	1033	4.86	<0.18
	919	4.86	<1.16
SN 1984E	4121	1.425	<0.073
SN 1985F	488	4.86	<0.33
	7140	8.46	<0.037
	353	4.86	<0.189
SN 1985G	51	4.86	<0.212
	168	4.86	<0.675
	638	4.86	<0.623
SN 1985H	25	4.85	<0.155
	1025	4.86	<0.3
SN 1987F	1006	4.86	<0.43
	1363	4.8	<0.18
	1059	4.8	<0.18
	2132	4.9	<0.09
SN 1987K	2394	8.44	<0.225
	45	1.66	<2.6
	875	4.86	<0.634
SN 1987M	5891	8.46	<0.034

Note. Δt is the time in days since explosion, ν is the observed frequency in GHz, and F_ν is the 3σ upper limit on the radio flux density.
Table 2 is published in its entirety in the machine-readable format. A portion is shown here for guidance regarding its form and content.

(This table is available in its entirety in machine-readable form in the online article.)

Table 3
Peaks of the Radio Emission

Name	Δt (days)	ν (GHz)	$F_{\rm p}$ (mJy)
SN 1979C	964.0	1.49	9.29
SN 1980K	116.0	5.0	2.28
SN 1981K	1480.0	1.5	1.28
SN 1983N	13.3	5.0	36.7
SN 1984L	<112.0	1.5	>1.01
SN 1985L	335.0	4.86	0.897
SN 1986E	245.0	4.86	>0.304
SN 1986J	1416.0	4.86	124.7

Note. When a peak in the light curve or spectrum is given, we estimate the peak flux density, time, and frequency as described in Section 4. When the peak is not observed we provide a lower limit on the peak flux density. If the lower limit is given from a spectrum, we set the time of observation as the time of the peak, Δt, and provide a limit on the peak frequency, ν. If the lower limit is given from a light curve, we set the frequency of observation, ν, as the peak frequency, and provide a limit on the time of the peak, Δt.
Table 3 is published in its entirety in the machine-readable format. A portion is shown here for guidance regarding its form and content.

(This table is available in its entirety in machine-readable form in the online article.)

ORCID iDs

Itai Sfaradi https://orcid.org/0000-0003-0466-3779
Assaf Horesh https://orcid.org/0000-0002-5936-1156
Joe Bright https://orcid.org/0000-0002-7735-5796
Dave A. Green https://orcid.org/0000-0003-3189-9998

References

Anderson, G. E., Horesh, A., Mooley, K. P., et al. 2017, MNRAS, 466, 3648
Argo, M. K., Beswick, R. J., Muxlow, T. W. B., & Pedlar, A. 2007, ATel, 1084
Barniol Duran, R., Nakar, E., & Piran, T. 2013, ApJ, 772, 78
Berger, E., Kulkarni, S. R., & Chevalier, R. A. 2002, ApJL, 577, L5
Beswick, R. J., Fenech, D., Thrall, H., et al. 2005, IAUC, 8572, #1
Beswick, R. J., Muxlow, T. W. B., Argo, M. K., & Pedlar, A. 2004a, IAUC, 8332, #2
Beswick, R. J., Muxlow, T. W. B., Argo, M. K., Pedlar, A., & Marcaide, J. M. 2004b, IAUC, 8435, #3
Bietenholz, M., & Bartel, N. 2007, ATel, 1254
Bietenholz, M., & Bartel, N. 2008a, ATel, 1525
Bietenholz, M., & Bartel, N. 2008b, ATel, 1657
Bietenholz, M., & Bartel, N. 2014, ATel, 6429
Bietenholz, M. F., Bartel, N., Argo, M., et al. 2021, ApJ, 908, 75
Bietenholz, M. F., Kamble, A., Margutti, R., Milisavljevic, D., & Soderberg, A. 2018, MNRAS, 475, 1756
Bose, S., Sutaria, F., Kumar, B., et al. 2015, ApJ, 806, 160
Cao, Y., Kasliwal, M. M., Arcavi, I., et al. 2013, ApJL, 775, L7
Chakraborti, S., & Ray, A. 2008, ATel, 1605
Chakraborti, S., Soderberg, A., Chomiuk, L., et al. 2015, ApJ, 805, 187
Chandra, P. 2018, SSRv, 214, 27
Chandra, P., Chakraborti, S., & Ray, A. 2007, ATel, 1082
Chandra, P., Chevalier, R. A., Chugai, N., et al. 2012, ApJ, 755, 110
Chandra, P., Chevalier, R. A., Chugai, N., Fransson, C., & Soderberg, A. M. 2015, ApJ, 810, 32
Chandra, P., Ray, A., & Bhatnagar, S. 2002, BASI, 30, 755
Chandra, P., & Soderberg, A. 2007, ATel, 1271
Chandra, P., & Soderberg, A. 2008, ATel, 1359
Chandra, P., & Soderberg, A. 2009a, ATel, 1891
Chandra, P., & Soderberg, A. 2009b, ATel, 2351
Chandra, P., Stockdale, C., Weiler, K., et al. 2008, ATel, 1465
Chandra, P., Stockdale, C. J., Chevalier, R. A., et al. 2009, ApJ, 690, 1839
Chevalier, R. A. 1981, ApJ, 251, 259
Chevalier, R. A. 1998, ApJ, 499, 810
Chevalier, R. A., & Fransson, C. 2006, ApJ, 651, 381
Chevalier, R. A., & Fransson, C. 2017, in Handbook of Supernovae, ed. A. W. Alsabti & P. Murdin (Berlin: Springer), 875
Chevalier, R. A., & Soderberg, A. M. 2010, ApJL, 711, L40
Corsi, A., Ofek, E. O., Frail, D. A., et al. 2010, ATel, 2915
de Jager, C., Nieuwenhuijzen, H., & van der Hucht, K. A. 1988, A&AS, 72, 259
DeMarchi, L., Margutti, R., Dittman, J., et al. 2022, ApJ, 938, 84
Dessart, L., Blondin, S., Brown, P. J., et al. 2008, ApJ, 675, 644
Drout, M. R., Milisavljevic, D., Parrent, J., et al. 2016, ApJ, 821, 57
Dwarkadas, V. V., Romero-Cañizales, C., Reddy, R., & Bauer, F. E. 2016, MNRAS, 462, 1101
Eck, C. R., Cowan, J. J., Boffi, F. R., & Branch, D. 1996, ApJL, 472, L25
Elmhamdi, A., Tsvetkov, D., Danziger, I. J., & Kordi, A. 2011, ApJ, 731, 129
Filippenko, A. V. 1997, ARA&A, 35, 309
Fox, O. D., Smith, N., Ammons, S. M., et al. 2015, MNRAS, 454, 4366
Gal-Yam, A. 2017, in Handbook of Supernovae, ed. A. W. Alsabti & P. Murdin (Berlin: Springer), 195
Gal-Yam, A., Leonard, D. C., Fox, D. B., et al. 2007, ApJ, 656, 372
Hickish, J., Razavi-Ghods, N., Perrott, Y. C., et al. 2018, MNRAS, 475, 5677
Horesh, A., Cao, Y., Mooley, K., & Carpenter, J. 2013a, ATel, 5198
Horesh, A., Kasliwal, M., Carpenter, J., et al. 2011, ATel, 3512
Horesh, A., Kulkarni, S. R., Corsi, A., et al. 2013b, ApJ, 778, 63
Horesh, A., Stockdale, C., Fox, D. B., et al. 2013c, MNRAS, 436, 1258
Horesh, A., Sfaradi, I., Ergon, M., et al. 2020, ApJ, 903, 132
Irani, I., Morag, J., Gal-Yam, A., et al. 2023, arXiv:2310.16885
Kamble, A., & Soderberg, A. 2013, ATel, 5154
Kamble, A., Soderberg, A. M., Chomiuk, L., et al. 2014, ApJ, 797, 2
Kamble, A., Margutti, R., Soderberg, A. M., et al. 2016, ApJ, 818, 111
Kelley, M. T., Stockdale, C. J., Sramek, R. A., et al. 2006, CBET, 495
Kimani, N., Sendlinger, K., Brunthaler, A., et al. 2016, A&A, 593, A18
Krauss, M. I., Soderberg, A. M., Chomiuk, L., et al. 2012, ApJL, 750, L40

Lacey, C. K., Van Dyk, S. D., Weiler, K. W., et al. 1999, IAUC, 7336, #2
Lacey, C. K., Weiler, K. W., Sramek, R. A., & van Dyk, S. D. 1998, IAUC, 7068, #2
Langer, N. 2012, ARA&A, 50, 107
Lundqvist, P., & Fransson, C. 1988, A&A, 192, 221
Margutti, R., Milisavljevic, D., Soderberg, A. M., et al. 2014, ApJ, 797, 107
McMullin, J. P., Waters, B., Schiebel, D., Young, W., & Golap, K. 2007, in ASP Conf. Ser. 376, Astronomical Data Analysis Software and Systems XVI, ed. R. A. Shaw, F. Hill, & D. J. Bell (San Francisco, CA: ASP), 127
Milisavljevic, D., Margutti, R., Soderberg, A. M., et al. 2013, ApJ, 767, 71
Misra, K., Pooley, D., Chandra, P., et al. 2007, MNRAS, 381, 280
Montes, M. J., Van Dyk, S. D., Weiler, K. W., Sramek, R. A., & Panagia, N. 1997, ApJ, 482, L61
Montes, M. J., Van Dyk, S. D., Weiler, K. W., Sramek, R. A., & Panagia, N. 1998, ApJ, 506, 874
Nayana, A. J., & Chandra, P. 2018, ATel, 11350
Nayana, A. J., Chandra, P., & Ray, A. K. 2018, ApJ, 863, 163
Nayana, A. J., Margutti, R., Wiston, E., et al. 2024, arXiv:2411.02647
Pacholczyk, A. G. 1970, Radio Astrophysics. Nonthermal Processes in Galactic and Extragalactic Sources (San Francisco, CA: Freeman), 1970
Pérez-Torres, M. A., Alberdi, A., Colina, L., et al. 2009, MNRAS, 399, 1641
Perrott, Y. C., Scaife, A. M. M., Green, D. A., et al. 2013, MNRAS, 429, 3330
Pooley, D., Lewin, W. H. G., Fox, D. W., et al. 2002a, ApJ, 572, 932
Pooley, D., Lewin, W. H. G., Fox, D. W., et al. 2002b, ApJ, 572, 932
Pooley, G. G., & Green, D. A. 1993, MNRAS, 264, L17
Romero-Cañizales, C., Herrero-Illana, R., Pérez-Torres, M. A., et al. 2014, MNRAS, 440, 1067
Romero-Canizales, C., Perez-Torres, M. A., Alberdi, A., et al. 2011, ATel, 3291
Rose, K., Horesh, A., Murphy, T., et al. 2024, MNRAS, 534, 3853
Roy, R., Kumar, B., Maund, J. R., et al. 2013, MNRAS, 434, 2032
Ryder, S., Kool, E., Kankare, E., et al. 2018, ATel, 11224
Ryder, S. D., Kool, E. C., Filipovic, M., et al. 2019, ATel, 12373
Ryder, S. D., Sadler, E. M., Subrahmanyan, R., et al. 2004, MNRAS, 349, 1093
Ryder, S. D., Stockdale, C. J., Immler, S., et al. 2011, ATel, 3764
Salamanca, I., Terlevich, R. J., & Tenorio-Tagle, G. 2002, MNRAS, 330, 844
Schinzel, F. K., Taylor, G. B., Stockdale, C. J., Granot, J., & Ramirez-Ruiz, E. 2009, ApJ, 691, 1380
Scott, M. A., & Readhead, A. C. S. 1977, MNRAS, 180, 539
Sfaradi, I., Horesh, A., Sollerman, J., et al. 2024, A&A, 686, A129
Shivvers, I., Zheng, W., Van Dyk, S. D., et al. 2017, MNRAS, 471, 4381
Smith, N. 2014, ARA&A, 52, 487
Smith, N. 2017, in Handbook of Supernovae, ed. A. W. Alsabti & P. Murdin (Berlin: Springer), 403
Smith, N., Li, W., Miller, A. A., et al. 2011, ApJ, 732, 63
Smith, N., Kilpatrick, C. D., Mauerhan, J. C., et al. 2017, MNRAS, 466, 3021
Soderberg, A. 2008, ATel, 1811
Soderberg, A., Kulkarni, S., & Frail, D. 2003, GCN, 2435, #1
Soderberg, A., Chandra, P., Stockdale, C., et al. 2008, ATel, 1455
Soderberg, A. M., Brunthaler, A., Nakar, E., Chevalier, R. A., & Bietenholz, M. F. 2010a, ApJ, 725, 922
Soderberg, A. M., Chevalier, R. A., Kulkarni, S. R., & Frail, D. A. 2006a, ApJ, 651, 1005
Soderberg, A. M., & Kulkarni, S. R. 2005, ATel, 571
Soderberg, A. M., Kulkarni, S. R., Berger, E., et al. 2005a, ApJ, 621, 908
Soderberg, A. M., Kulkarni, S. R., & Frail, D. A. 2004, ATel, 351
Soderberg, A. M., Kulkarni, S. R., & Frail, D. A. 2005b, ATel, 621
Soderberg, A. M., Nakar, E., Berger, E., & Kulkarni, S. R. 2006b, ApJ, 638, 930
Soderberg, A. M., Chakraborti, S., Pignata, G., et al. 2010b, Natur, 463, 513
Soderberg, A. M., Margutti, R., Zauderer, B. A., et al. 2012, ApJ, 752, 78
Sokolovsky, K., Giroletti, M., Stagni, M., Nanni, M., & Mahabal, A. 2013, ATel, 5264
Srinivasaragavan, G. P., Sfaradi, I., Jencson, J., et al. 2022, A&A, 660, A138
Stockdale, C. J., Kelley, M., van Dyk, S. D., et al. 2005, IAUC, 8603, #2
Stockdale, C. J., Sramek, R. A., Van Dyk, S. D., Weiler, K. W., & Panagia, N. 2003a, IAUC, 8153, #2
Stockdale, C. J., Van Dyk, S. D., Sramek, R. A., et al. 2004a, IAUC, 8282, #2
Stockdale, C. J., Weiler, K. W., Immler, S., et al. 2008a, IAUC, 8939, #2
Stockdale, C. J., Weiler, K. W., Immler, S., et al. 2008b, CBET, 1299, #1
Stockdale, C. J., Weiler, K. W., Immler, S., et al. 2008c, ATel, 1883
Stockdale, C. J., Weiler, K. W., Immler, S., et al. 2008d, ATel, 1915
Stockdale, C. J., Weiler, K. W., Soderberg, A., et al. 2008e, ATel, 1452
Stockdale, C. J., Weiler, K. W., Van Dyk, S. D., et al. 2003b, ApJ, 592, 900
Stockdale, C. J., Weiler, K. W., van Dyk, S. D., et al. 2004b, IAUC, 8415, #1
Stockdale, C. J., Weiler, K. W., Immler, S., et al. 2009a, ATel, 1923
Stockdale, C. J., Weiler, K. W., Immler, S., et al. 2009b, ATel, 1912
Stritzinger, M., Mazzali, P., Phillips, M. M., et al. 2009, ApJ, 696, 713
Utrobin, V. P., & Chugai, N. N. 2013, A&A, 555, A145
van der Horst, A. J., Kamble, A. P., Paragi, Z., et al. 2010, ATel, 2612
van der Horst, A. J., Kamble, A. P., Paragi, Z., et al. 2011, ApJ, 726, 99
Van Dyk, S. D., Lacey, C. K., Sramek, R. A., & Weiler, K. W. 1999, IAUC, 7322, #2
van Dyk, S. D., Montes, M. J., Weiler, K. W., Sramek, R. A., & Panagia, N. 1998, ApJ, 115, 1103
van Dyk, S. D., Sramek, R. A., Weiler, K. W., Montes, M. J., & Panagia, N. 1996, IAUC, 6378, #2
van Dyk, S. D., Sramek, R. A., Weiler, K. W., & Panagia, N. 1993, ApJ, 409, 162
van Dyk, S. D., Weiler, K. W., Sramek, R. A., & Panagia, N. 1992, ApJ, 396, 195
Vink, J. S. 2022, ARA&A, 60, 203
Vink, J. S., de Koter, A., & Lamers, H. J. G. L. M. 2001, A&A, 369, 574
Weiler, K. W., Panagia, N., & Montes, M. J. 2001, ApJ, 562, 670
Weiler, K. W., Panagia, N., Montes, M. J., & Sramek, R. A. 2002, ARA&A, 40, 387
Weiler, K. W., Panagia, N., & Sramek, R. A. 1990, ApJ, 364, 611
Weiler, K. W., Panagia, N., Stockdale, C., et al. 2011, ApJ, 740, 79
Weiler, K. W., Sramek, R. A., Panagia, N., van der Hulst, J. M., & Salvati, M. 1986, ApJ, 301, 790
Weiler, K. W., van Dyk, S. D., Panagia, N., Sramek, R. A., & Discenna, J. L. 1991, ApJ, 380, 161
Weiler, K. W., Williams, C. L., Panagia, N., et al. 2007, ApJ, 671, 1959
Wellons, S., & Soderberg, A. M. 2011, BAAS, 43, 337.15
Williams, C. L., Panagia, N., Van Dyk, S. D., et al. 2002, ApJ, 581, 396
Yadav, N., Ray, A., Chakraborti, S., et al. 2014, ApJ, 782, 30
Yaron, O., Perley, D. A., Gal-Yam, A., et al. 2017, NatPh, 13, 510
Zauderer, A., Kamble, A., Chakraborti, S., & Soderberg, A. 2013, ATel, 4866
Zwart, J. T. L., Barker, R. W., Biddulph, P., et al. 2008, MNRAS, 391, 1545